



Enhancement of rutile phase formation in TiO₂ films deposited on stainless steel substrates with a vacuum arc



L.M. Franco Arias^a, A. Kleiman^a, D. Vega^{b,c}, M. Fazio^a, E. Halac^{b,c}, A. Márquez^{a,*}

^a Instituto de Física del Plasma, CONICET, Departamento de Física, Facultad de Ciencias Exactas y Naturales, Universidad de Buenos Aires, Cdad. Universitaria Pab. 1, 1428, Buenos Aires, Argentina

^b Departamento Física de la Materia Condensada, Gerencia de Investigación y Aplicaciones, Comisión Nacional de Energía Atómica, Av. Gral Paz, 1499 San Martín, Buenos Aires, Argentina

^c Escuela de Ciencia y Tecnología, Universidad Nacional de San Martín, Provincia de Buenos Aires, Argentina

ARTICLE INFO

Article history:

Received 29 December 2015

Received in revised form 5 July 2017

Accepted 18 July 2017

Available online 25 July 2017

Keywords:

Titanium dioxide

Rutile

Cathodic arc

Austenitic stainless steel

ABSTRACT

The rutile phase of TiO₂ has raised a wide interest for biomaterial applications. Since rutile is generally synthesized at high temperatures, a deposition process based on a cathodic arc discharge has been investigated in order to obtain rutile coatings at lower temperature on stainless steel substrates. In this work, TiO₂ films were deposited on AISI 316 L stainless steel substrates heated at 300 and 400 °C with a negative bias of 120 V, employing Ti interlayers of different thicknesses. TiO₂ films of approximately 500 and 900 nm were grown on Ti interlayers with thicknesses in the range 0–550 nm. The effect of Ti interlayers on the crystalline structure of TiO₂ coatings was systematically studied with X-ray diffraction and Raman spectroscopy. The introduction of the Ti layer increased the rutile/anatase proportion either at 300 or 400 °C, turning rutile into the main phase in the TiO₂ film. The largest amount of rutile for both temperatures was attained with a 55 nm Ti interlayer, the thinnest thickness studied.

© 2017 Published by Elsevier B.V.

1. Introduction

Titanium dioxide is a material known to be non-toxic and to have excellent chemical stability and good mechanical properties [1]. It also exhibits high hydrophilicity [2] and good photocatalytic properties under UV irradiation [3]. Besides, titanium oxide coatings have been found to improve biocompatibility and hemocompatibility on prosthesis [4–6] while, in addition, increase hardness and wear resistance [7]. It was found that the rutile phase of TiO₂ can decrease the rate of dissolution of metal ions in a body fluid, and is chemically more stable than anatase, either at high or low pH [8]. These features turn rutile TiO₂ films into a very attractive coating for biomaterial applications.

TiO₂ films have been produced by a great variety of techniques; among them cathodic arc deposition (CAD) has demonstrated to be an efficient method for the deposition of films with good adhesion to the substrate [9]. Cathodic arcs are characterized by the production of metallic plasma with high degree of ionization and ions with high kinetic energy [10]. The ion energy for arc generated Ti⁺ is about 40–50 eV [11,12] and can be increased by applying a negative bias to the substrate. However, the mean energy of the metal particles impinging on the surface may be lowered by collisions and reactions with the gas [13]. The particle energy and the substrate temperature have significant influence on the film microstructure; according to the phase diagram

proposed by Löbl et al. for the synthesis of TiO₂ [14], rutile phase is obtained at 300 °C with ion energy above 10 eV, while at room temperature ion energy should be higher than 40 eV.

Most studies on TiO₂ synthesized by CAD focused on the characterization of films deposited on Si (100) and glass substrates. Generally, deposition at room temperature and without bias led to the formation of amorphous films. In turn, anatase phase was obtained with substrate temperature above 300 °C [15,16]. Nonetheless, anatase films were also reported for films grown at room temperature on silicon substrates [17]. On the other hand, films grown in rutile phase were reported for silicon substrates negatively biased above 100 V, either at room temperature [17] or at 300 °C [18], with O₂ pressure in the range 0.2–0.4 Pa. Anatase and rutile coatings were also obtained after post-deposition annealing of amorphous samples at 400 °C [15] and 800 °C [11], respectively; while intermediate temperatures led to mixed samples [16]. In contrast, films synthesized by sol-gel required annealing at 700 °C to transform to anatase and 1000 °C to rutile [19].

Austenitic stainless steel has been extensively used in several industries due to its excellent corrosion resistance. Typical applications include medical implants like pins, screws and orthopedic implants. TiO₂ films grown with a vacuum arc on various substrates, including AISI 304 L austenitic stainless steel, were reported in [20]. In that work, authors employed different arc configurations leading to different deposition rates; substrates were biased up to 120 V with the temperature reaching values in the range 150–300 °C after 10 min deposition without additional heating. Based on Raman studies, authors assert

* Corresponding author.

E-mail address: amarquez@df.uba.ar (A. Márquez).

that films obtained on stainless steel substrates grew in rutile phase when deposition rate was the highest (60 nm/min). However, X-ray diffraction (XRD) studies in glancing incidence geometry showed that rutile peaks were not clearly defined. In a previous work of our group [21], TiO₂ films were grown by CAD on AISI 316 L stainless steel substrates biased at 120 V; the temperature reaching ~60 °C after 2 min deposition, with a deposition rate of 170 nm/min. Although Raman spectra revealed the presence of anatase and rutile, studying different regions of the surface demonstrated that the crystals were present in small areas, the films being mainly amorphous. For these films no peaks were detected by XRD, in agreement with a mostly amorphous film. When the substrates were kept at 300 °C with bias in the range 0–120 V the anatase and rutile peaks observed by XRD were not well defined. Despite the relatively low intensity of the TiO₂ peaks, it was noticed that anatase was the main phase for most of the samples, the rutile proportion increasing when biasing at –120 V. This fact indicated that the bias favors the nucleation of rutile as the energy of the ions impinging on the surface was increased.

Films prepared by magnetron sputtering on surgical AISI 316 L austenitic stainless steel at 300 °C grew in anatase phase; while the introduction of a Ti interlayer between the stainless steel substrate and the TiO₂ film led to crystallization in rutile phase, and also enhanced the surface hardness and corrosion resistance [22].

The aim of this work was to synthesize TiO₂ films by CAD on austenitic stainless steel substrates toward their future application on biocompatible surfaces. For this purpose, the effect of Ti interlayers on the crystalline structure of TiO₂ coatings was studied, so as to enhance the rutile phase growth at a lower temperature than that employed for crystallization in post-deposition annealing.

2. Experiment

The cathodic arc device used for the synthesis of the films has been described in detail in a previous work [23]. The arc was run at a current of 110 A between a titanium cathode and the stainless steel vacuum chamber which acts as the anode. A Ti grade 2 (99.5% purity) cylinder of 55 mm in diameter and 40 mm in height was employed as cathode. The base pressure of the system was below 0.1 Pa. AISI 316 L austenitic stainless steel substrates (2.5 cm diameter, 0.1 cm thickness) were placed at 26 cm from the cathode surface on an electrically insulated heater. The current in the resistive heater was controlled by means of a Novus N2000 universal process controller to fix the required temperature. Sample temperature was measured during deposition with an insulated K-type thermocouple attached to the back side of the substrate. The substrate temperature was held with an accuracy of 10%.

For deposition of Ti films, the arc was run in vacuum (pressure < 0.1 Pa) varying the deposition time in the range 15–150 s in order to attain Ti layers with different thicknesses. TiO₂ films were grown by running the arc in an oxygen atmosphere with a gas inlet flow of 60 sccm (pressure in the range 5–8 Pa) during 270 s and 480 s. Bilayer Ti/TiO₂ films were obtained by successive deposition of Ti and TiO₂ in the mentioned conditions. After completing the set time for Ti deposition, the oxygen inlet was open without interrupting the discharge, the working pressure for TiO₂ deposition being established in approximately 10 s. All films were deposited keeping the sample at constant temperature during the whole process, 300 and 400 °C, with negative bias of 120 V. Details on all the employed deposition conditions can be found in Table 1.

All samples were weighed on an analytical scale (Ohaus AS200) before and after deposition with the aim of determining the deposited mass. The depth profile of the films was analyzed for some of the samples with scanning electron microscopy (SEM) (FEG-SEM Zeiss Leo 982 GEMINI) after cutting them.

The crystalline structure of the films was examined by XRD (Panalytical Empyrean with PixCel 3D detector) with a CuK_α source,

Table 1
Deposition conditions employed for Ti interlayers and TiO₂ films.

Deposition condition	Deposition time (s)		T (°C)	Bias (V)
	Ti	TiO ₂		
1	–	270	300	–120
2	15	270	300	–120
3	30	270	300	–120
4	90	270	300	–120
5	150	270	300	–120
6	–	270	400	–120
7	15	270	400	–120
8	30	270	400	–120
9	90	270	400	–120
10	150	270	400	–120
11	–	480	400	–120
12	15	480	400	–120
13	150	480	400	–120
14	15	–	400	–120
15	30	–	400	–120
16	90	–	400	–120
17	150	–	400	–120

in the Bragg-Brentano geometry with a 0.026° 2θ step and in parallel beam geometry (glancing incidence) with an elliptic mirror in the incident beam using an incidence angle of 0.5° and a step of 0.03°, for 2θ between 20 and 60°. Residual stresses of the Ti films were analyzed from glancing incidence XRD patterns using the multiple {hkl} method [24]. Measurements were performed with an incidence angle (ω) of 1° for 2θ between 20 and 115°. The texture of TiO₂ films was studied by measuring a Bragg reflection and systematically changing the incidence (ω), tilt (χ) and in plane rotation (ψ) angles.

Raman spectra were recorded on a LabRAM HR Raman system (Horiba Jobin Yvon), equipped with two monochromator gratings and a charge coupled device detector. An 1800 g/mm grating and a 100 μm hole result in a spectral resolution of 1.5 cm⁻¹. The spectrograph was coupled to an imaging microscope with 10×, 50×, and 100× magnification. The He-Ne laser line at 632.8 nm was used as excitation source and was filtered to give a laser power or density at the exit of the objective lens varying from 0.1 to 1 W/mm². Several measurements were performed, adjusting the laser fluence, to ensure that the heating produced by the laser was minimized and that the sample was not altered. Measurements were taken in a backscattering geometry, with a 100× magnification and the spot size was approximately 10 μm. For all the measured spectra, 4 accumulations of 60 s were recorded.

3. Results

3.1. Deposition rate

Deposited masses of Ti and TiO₂ were determined from the average gain weight of at least 10 samples coated with Ti and other 10 samples coated with TiO₂. The Ti film density was assumed as the Ti bulk density (4.5 g/cm³) to calculate the deposition rate, obtaining a value of (3.5 ± 0.3) nm/s. The deposition rate of TiO₂ was calculated taking a density value of 3.9 g/cm³, which corresponds to the mean value among amorphous TiO₂ (3.6 g/cm³), anatase (3.89 g/cm³) and rutile (4.23 g/cm³) bulk densities, and resulted in (1.8 ± 0.2) nm/s. Film thicknesses for different deposition times were estimated from the mentioned deposition rates. The calculated thicknesses (with uncertainty of ~10%) for Ti films deposited during 15, 30, 90 and 150 s were 55, 105, 315 and 525 nm, respectively; while mean values for TiO₂ film thickness deposited during 270 and 480 s were 485 and 865 nm. For all the bilayer films the gain weight agreed within the uncertainty with the expected value according to Ti and TiO₂ deposition rates.

The thickness of bilayer films was checked through depth profile images obtained by SEM. Images were taken with different

magnifications and at several places along the film. Measurements of thicknesses using different magnification at the same place gave results with differences up to 8%, while dispersion in the values was approximately 10% when measuring at several places. Typical pictures from bilayer films are shown in Fig. 1, these images were obtained from a sample deposited in condition 3 of Table 1. Two compact layers can be observed in the picture (Fig. 1a). The layer on the substrate (interlayer) corresponds to the Ti film with a thickness of 110 nm. The second layer, corresponding to the TiO₂ film, presents a thickness of approximately 440 nm. The TiO₂ layer exhibits a columnar structure which can be more clearly observed in Fig. 1b. For this sample, considering measurements from several SEM images, the average thickness was (107 ± 8) nm for the Ti interlayer and (470 ± 40) nm for the TiO₂ film. Thickness measurements from SEM agreed with the thickness values determined from mass measurements taking into account uncertainties associated to each method.

3.2. Characterization of Ti films

Titanium films with the same thicknesses employed for the bilayer coatings were prepared by CAD. Their structure was studied by XRD. Fig. 2 show signals obtained in Bragg-Brentano geometry from films deposited at 400 °C and biased at -120 V, displaying the angular region where Ti peaks were observed. For Ti layers of 55 and 105 nm only small peaks corresponding to (100) and (101) planes can be observed. For higher thicknesses (315 and 525 nm)

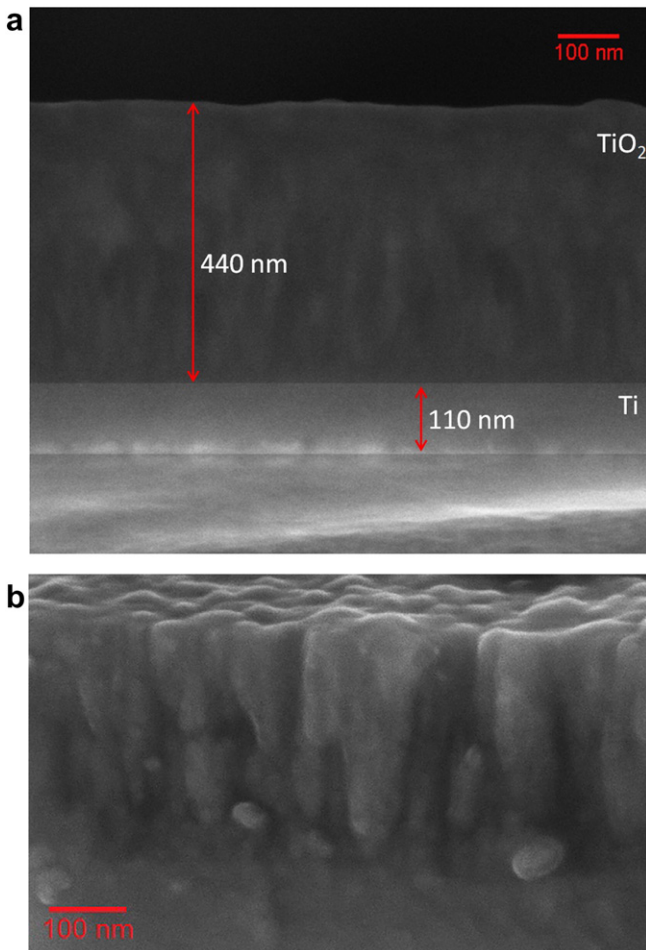


Fig. 1. Depth profile SEM image of a bilayer film deposited in condition 3 showing (a) the thickness of both layers and (b) the columnar structure of the TiO₂ layer.

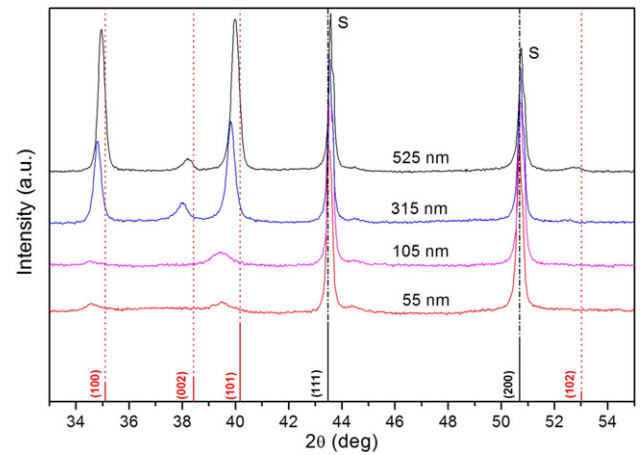


Fig. 2. XRD patterns from Ti films of different thickness grown on stainless steel at 400 °C and biased at -120 V. Patterns measured in Bragg-Brentano geometry. Bragg peaks of Ti and of austenite corresponding to the substrate (S) are indicated as a reference.

the peak corresponding to the (002) plane is also observed. It can be noticed that the Ti peaks are shifted to lower angles with respect to the reference pattern corresponding to the hcp Ti lattice (ICDD card No. 00-044-1294). This effect is more pronounced for thinner layers. Using the Bragg equation the Ti lattice parameters were calculated. The obtained parameters are depicted as a function of the Ti layer thickness in Fig. 3. Both parameters decreased as the thickness increased, being always above the values corresponding to the reference Ti lattice (indicated with solid lines in Fig. 3). In order to evaluate whether the cell expansion is caused by stresses, Ti films of 55 and 525 nm were analyzed by XRD in glancing incidence. The obtained patterns are presented in Fig. 4. Only peaks corresponding to Ti and the substrate are noticeable. Defining the elastic strain (ϵ) as:

$$\epsilon = \frac{d_{hkl} - d_{hkl}^0}{d_{hkl}^0} \quad (1)$$

where d_{hkl} denotes the lattice spacing - obtained from the measured pattern - and d_{hkl}^0 is the strain-free lattice spacing. Film stress was studied using the multiple $\{hkl\}$ method through ϵ vs. $\sin^2\psi$ plots, with $\psi = \theta^{hkl} - \omega$ [24,25]. For elastically isotropic crystallites and a rotationally symmetric biaxial stress state, a linear trend is expected,

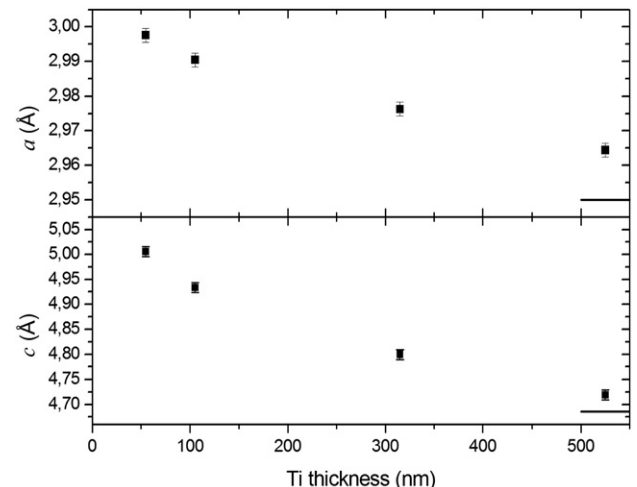


Fig. 3. Lattice parameters of the Ti interlayer as a function of the layer thickness.

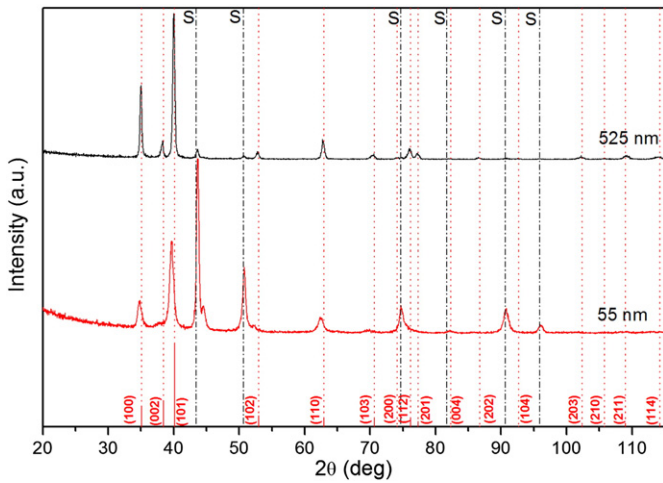


Fig. 4. Glancing incidence XRD patterns from Ti films of different thickness grown on stainless steel at 400 °C and biased at -120 V. Bragg peaks of Ti and of the substrate (S) are indicated as a reference.

the slope being proportional to the stress (σ). The equation that relates these variables can be expressed as:

$$\varepsilon = \left(2S_1 + \frac{1}{2}S_2 \sin^2 \psi \right) \sigma \quad (2)$$

with

$$S_1 = -\frac{\nu}{E}, S_2 = \frac{2(1+\nu)}{E} \quad (3)$$

where ν is the Poisson's ratio and E the elastic modulus. For each film two different ε were calculated, one deformation (ε_1) considering the reference hcp Ti cell and the other (ε_2) considering the expanded cell as the strain-free lattice. For the expanded lattice, d_{hkl}^0 were determined with the parameters calculated from Bragg-Brentano XRD patterns (Fig. 3). The graph is presented in Fig. 5. For the thickest Ti film a linear trend with a similar slope was observed in both ε_1 and ε_2 cases. Considering the ranges of ν and E reported for titanium [26], a compressive stress of (-0.45 ± 0.08) GPa was obtained. Therefore, the expected value for the intercept from Eqs. (2) and

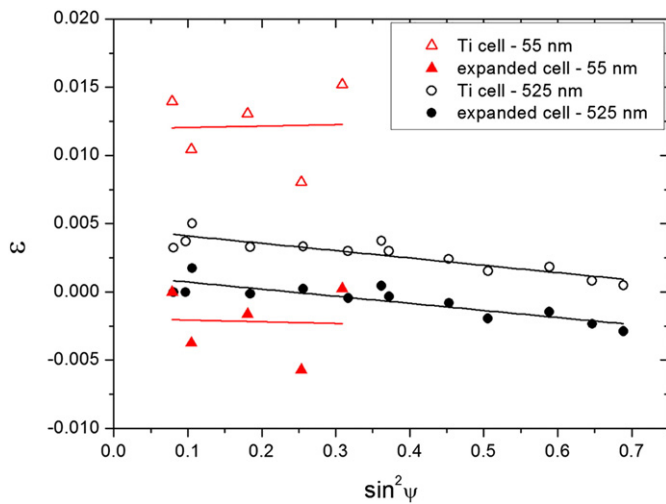


Fig. 5. ε vs $\sin^2 \psi$ plots for Ti films of different thickness corresponding to XRD patterns of Fig. 4. Elastic deformation ε calculated respect to the Ti lattice and the proposed expanded lattice.

(3) would be (0.0025 ± 0.0012) . The intercept values determined from the linear fitting were (0.0047 ± 0.0003) for ε_1 and (0.0013 ± 0.0004) for ε_2 . It can be noticed that the latter does not show significant differences with respect to the expected value. For the thinnest Ti film a conclusive trend associated with stress could not be determined because the number of identified peaks was low. However, the wide scattering of the ε data around a slope value close to zero would indicate a low stress, with an expected offset also close to zero. The offsets determined from a linear regression fitting were (0.012 ± 0.004) for ε_1 and (-0.002 ± 0.003) for ε_2 . This analysis indicates that the results obtained from ε_2 plots are more consistent with Eqs. (2) and (3) than those obtained from ε_1 plots. These results suggest that the lattice expansion cannot be attributed to the presence of compressive stresses which cause elastic deformation of the cell with respect to the expanded lattice.

A typical Raman spectrum from a 55 nm Ti film on stainless steel 316 L is shown in Fig. 6. Titanium does not have any Raman active modes; then the observed spectrum with the broad crest around 250 cm^{-1} can be associated to oxides present on the surface of the film.

3.3. X-ray diffraction study of Ti/TiO₂ films

X-ray diffractograms from TiO₂ films deposited at 300 °C on Ti layers of different thickness (deposition conditions 1–5) are plotted in Fig. 7. It can be seen that the sample without the Ti interlayer (0 nm) exhibited a small peak corresponding to anatase (101) and an even smaller peak of rutile (110). When the Ti interlayer was inserted rutile became the predominant phase. This effect was more noticeable for the thinnest Ti interlayer, for which the biggest rutile peak was obtained. Fig. 8 displays the patterns obtained in glancing incidence XRD from samples deposited in conditions 1, 2 and 5. This figure shows the same trend observed in Fig. 7 but with an enhanced intensity of the peaks corresponding to rutile and anatase, these peaks becoming more significant in comparison with those corresponding to the substrate and the titanium layer. Furthermore, peaks corresponding to rutile planes (101), (111), (211) and (310) are also appreciable in glancing incidence XRD, especially in the sample with the largest amount of rutile (55 nm Ti). Because of the observed similarities between $\theta - 2\theta$ and glancing incidence scans, no preferred orientation (texture) is expected.

Fig. 9 shows XRD signals obtained in Bragg-Brentano geometry from films deposited at 400 °C (deposition conditions 6–10). The structure observed in these films as a function of the Ti interlayer was similar to that exhibited in films grown at 300 °C, but the heights of the rutile peaks in Fig. 9 were relatively larger. For all deposition conditions XRD patterns exhibited the same angular positions for the rutile phase (i.e.

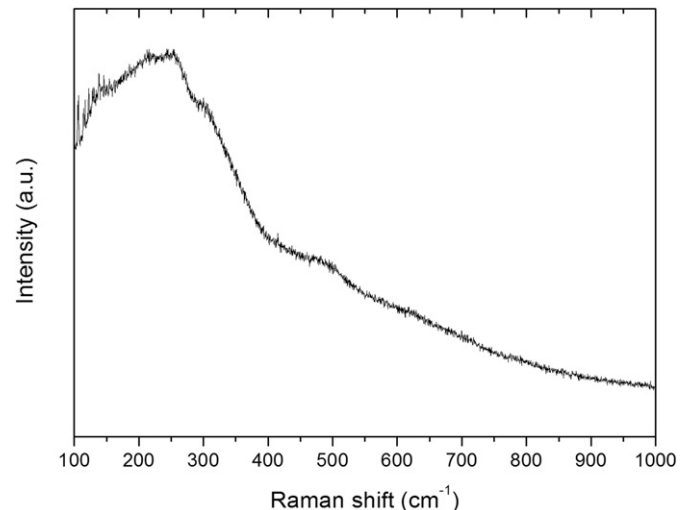


Fig. 6. Raman spectrum from a 55 nm Ti film on stainless steel 316 L.

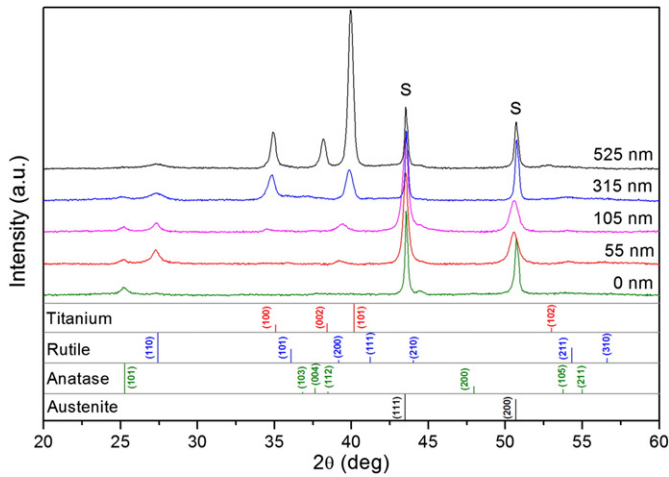


Fig. 7. XRD patterns from TiO₂ films of 485 nm grown at 300 °C on stainless steel (0 nm) and with Ti interlayers of 55, 105, 315 and 525 nm. Patterns measured in Bragg-Brentano geometry. Bragg peaks of anatase, rutile, Ti and austenite are indicated as a reference.

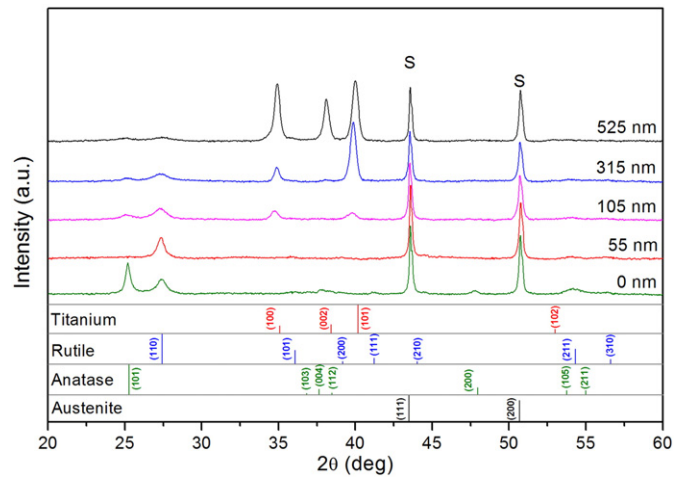


Fig. 9. XRD patterns from TiO₂ films of 485 nm grown at 400 °C on stainless steel (0 nm) and with Ti interlayers of 55, 105, 315 and 525 nm. Patterns measured in Bragg-Brentano geometry. Bragg peaks of anatase, rutile, Ti and austenite are indicated as a reference.

no shifts among different samples were observed). The 2θ-positions matched with the rutile reference pattern of the ICDD card No. 01-076-1940. Employing the Bragg equation, the distances between different planes were determined from the position of the peaks. Then, the lattice parameters were calculated, resulting $a = b = (4.613 \pm 0.004)$ Å and $c = (2.974 \pm 0.007)$ Å. On the other hand, the XRD patterns for samples grown at both temperatures showed that the peaks associated with the Ti interlayer were shifted to lower angles to the same extent as the shifts registered for the pure Ti films.

In order to evaluate the relative amount of the TiO₂ crystalline phases (rutile and anatase) as a function of the Ti interlayer thickness, TiO₂ XRD peaks were analyzed by Rietveld refinement. Before applying the Rietveld method, the absence of TiO₂ film texture was checked by comparing the intensity of the main peaks for both phases measuring at six different Euler angle configurations, maintaining the same diffraction angle step and same exposure time in each configuration. The signals registered from a sample coated in condition 8 (see Table 1) are depicted in Fig. 10. The relative peak intensities were similar for all the Euler angle configurations, confirming that the films exhibited no preferred orientation. Therefore, the refinement was applied employing the main XRD peaks of each phase, i.e. the peaks corresponding to the (101) anatase plane and to the (110) rutile plane. The contribution of

the rest of the peaks was not significant for any of the phases. This procedure was performed with the scale factors from anatase and rutile as free parameters. The results obtained from Rietveld refinement are depicted in Fig. 11a, the plotted values being the average of the rutile percentages obtained from three different samples for each deposition condition. TiO₂ films deposited on the substrate surface (0 nm Ti) presented the lowest percentages of rutile, approximately 50% for films deposited at 400 °C and 30% for films grown at 300 °C. With the addition of a thin Ti interlayer (55 nm), the proportion of rutile became the highest; in particular, no anatase has been detected by XRD in some of the samples obtained at 400 °C. For higher thicknesses of the Ti interlayer the percentage of rutile was almost constant for samples grown at 400 °C, while the proportion of rutile decreased for those deposited at 300 °C.

The amount of a crystalline phase in a film is related to the integrated intensity (area) of the associated XRD peaks. As the TiO₂ film thickness was the same for all the samples, the comparison of the areas allows to evaluate what deposition conditions most efficiently promoted the crystallization in rutile phase. The obtained rutile and anatase peak areas are presented in Fig. 11b and c, respectively. The amount of rutile

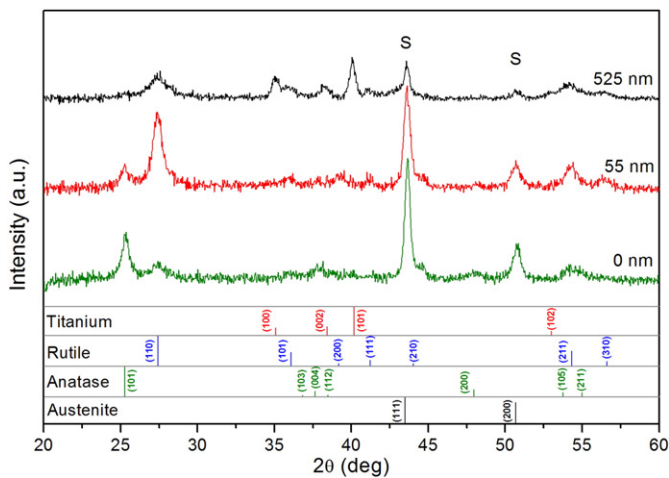


Fig. 8. Glancing incidence XRD patterns from TiO₂ films of 485 nm grown at 300 °C on stainless steel (0 nm) and with Ti interlayers of 55 and 525 nm. Bragg peaks of anatase, rutile, Ti and austenite are indicated as a reference.

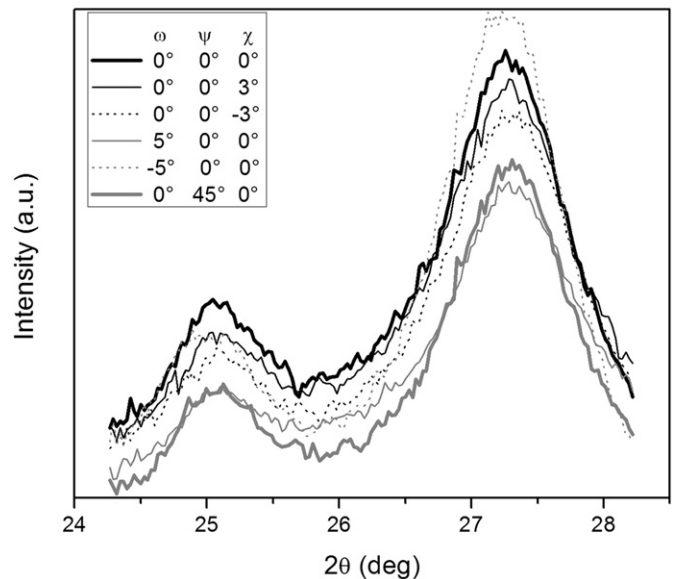


Fig. 10. Main TiO₂ XRD peaks for different Euler angle configurations. Signals correspond to a film grown in condition 8.

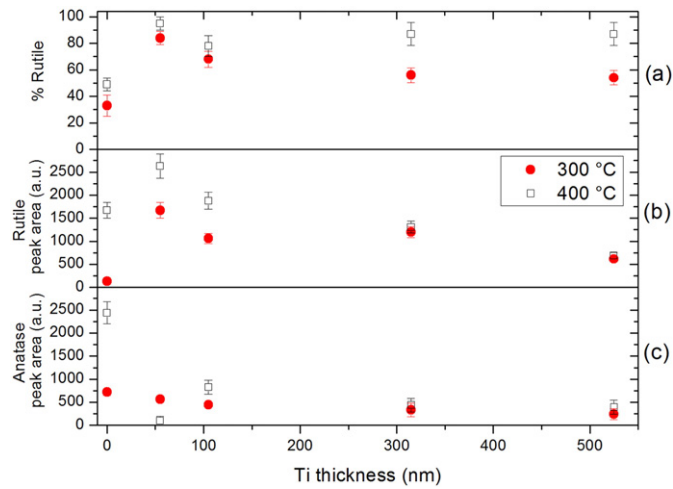


Fig. 11. Proportion of crystalline phases as a function of the Ti interlayer thickness: (a) rutile percentage obtained by Rietveld method, (b) XRD rutile peak area and (c) XRD anatase peak area.

was the largest when a Ti interlayer of 55 nm was employed, the area value being higher for 400 °C. The rutile peak area decreased as the Ti thickness increased for both temperatures. The anatase peak area showed the maximum value for films without Ti interlayer. Both crystalline phases presented a marked reduction for the thickest Ti interlayer. These samples were subjected to a post-deposition annealing at 700 °C during 3 h in vacuum. After the annealing the film presented a larger amount of crystallized TiO₂, mainly rutile. This indicated that on thick Ti interlayers fundamentally amorphous TiO₂ films were deposited.

Fig. 12 shows typical XRD diffractograms for thicker TiO₂ films (865 nm) deposited in conditions 11, 12 and 13. In these patterns, besides the rutile (110) peak, other peaks associated to different planes of the rutile lattice can be identified. Thus, all peaks were considered when applying the Reitveld method. The analysis revealed that films grown without Ti interlayer (0 nm) exhibited 86% of rutile, while with a 55-nm titanium interlayer the percentage increased to 97%. The dependence of the area of the rutile peaks on the Ti interlayer thickness presented a similar behavior to that observed for thinner TiO₂ films; the highest area value was found for the interlayer of 55 nm. The further enhancement on the rutile

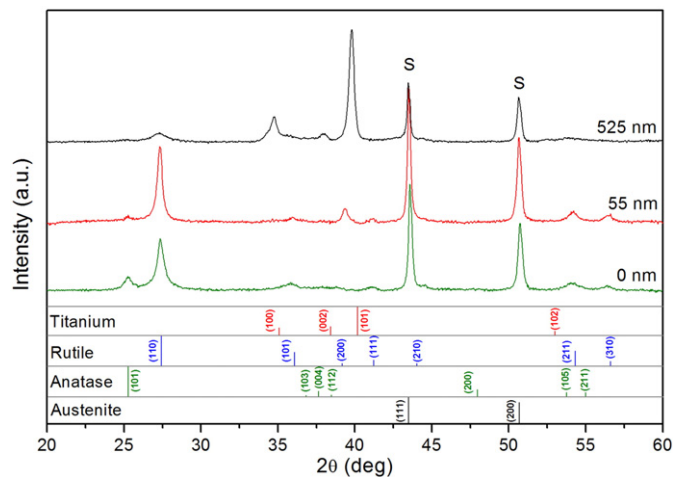


Fig. 12. XRD patterns from TiO₂ films of 865 nm grown at 400 °C on stainless steel (0 nm) and with Ti interlayers of 55 and 525 nm, deposition conditions 11, 12 and 13, respectively. Patterns measured in Bragg-Brentano geometry. Bragg peaks of anatase, rutile, Ti and austenite are indicated as a reference.

phase formation in thicker TiO₂ films might be attributed to the longer deposition time. The anatase to rutile phase transformation occurs gradually as a function of the heat treatment time [27], thus a longer process time - i.e. a longer heat treatment - could lead to a higher amount of rutile in the films.

3.4. Raman spectroscopy study of Ti/TiO₂ films

Raman spectra for films grown at 300 and 400 °C, without Ti interlayer and with a Ti layer of 55 nm, are shown in Fig. 13. Different measurements were taken across the surface of the samples to check for uniformity in the film structure as Raman probes a small area of the film in contrast with XRD measurements which average over a much larger area. The structure of the films was found to be uniform across the sample surface. Reference spectra for powder anatase and rutile are also plotted in Fig. 13. Anatase has six Raman active modes, an intense E_g peak at 144 cm⁻¹ followed by smaller peaks corresponding to E_g (197 cm⁻¹ and 640 cm⁻¹), B_{1g} (400 cm⁻¹) and A_{1g} + B_{1g} (515 cm⁻¹) modes. Rutile presents four vibration modes, E_g (447 cm⁻¹), A_{1g} (612 cm⁻¹) and with less intense peaks B_{1g} (143 cm⁻¹) and B_{2g} (826 cm⁻¹) [28]. This phase shows also a wide Raman peak at 235 cm⁻¹ due to multiple phonon scattering process [29,30].

TiO₂ films grown without the Ti interlayer show mainly anatase peaks (Fig. 13a). The Raman spectrum for the film grown at 300 °C displays a background signal which can be attributed to amorphous TiO₂.

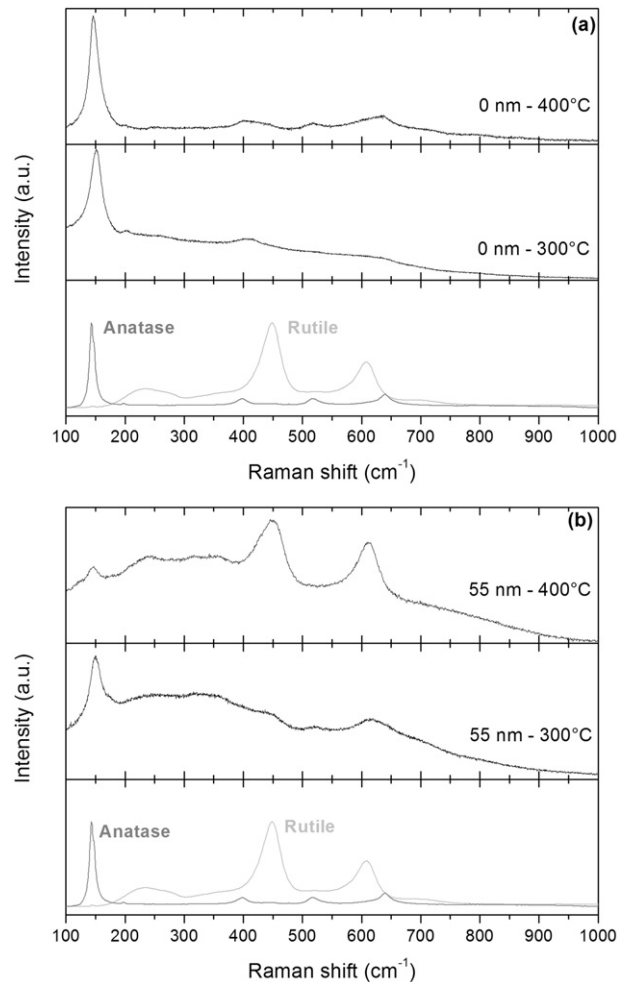


Fig. 13. Raman spectra from TiO₂ films deposited at 300 and 400 °C, (a) without Ti interlayer (0 nm) and (b) with a 55 nm Ti interlayer. Reference spectra from powder anatase and rutile are plotted.

The background is not present in the sample grown at 400 °C which suggests a higher degree of crystallization. The Raman spectra of TiO₂ films with a 55 nm Ti interlayer (Fig. 13b) display significant background signal, which corresponds well with the Raman spectra of a Ti film shown in Fig. 6. With the addition of the Ti interlayer the height of anatase peaks decreased while the amount of rutile increased, this enhancement being more pronounced for films deposited at 400 °C. The differences observed by Raman in the crystallization of TiO₂ with and without the Ti interlayer agreed with XRD results.

For samples deposited at 300 °C the main anatase E_g peak appeared at 150 cm⁻¹, while for samples grown at 400 °C, the peak position was 146 cm⁻¹ which means a slight shift respect to the reference. This effect was found for both types of films, with and without Ti interlayer. It can be noticed from Fig. 13a that the line width of the E_g mode for samples grown at 300 °C is twice the width of the anatase reference signal, and for samples deposited at 400 °C is similar to the reference.

4. Discussion

The results presented in Section 3 indicate that deposition at 400 °C and a thin Ti interlayer promoted the crystallization of TiO₂ in rutile phase.

Raman spectra in Fig. 13a showed the peak corresponding to the anatase E_g mode broadened and shifted to higher wave number for films grown at 300 °C, while samples obtained at 400 °C exhibited a line shape similar to the anatase reference. The position shift and the broadening can be attributed to the presence of oxygen defects, to a higher lattice strain and/or to a smaller crystallite size [30]. Then, the obtained results indicate that the higher temperature employed during the process led to a reduction in oxygen defects and/or to an increase in the crystallite size of anatase phase. Even so it is expected that the crystallite size has remained small; according to a previous work the crystallite size for anatase TiO₂ films grown by cathodic arc at 400 °C was estimated below 30 nm [16]. XRD results from films without Ti interlayer showed that increasing the temperature from 300 to 400 °C contributes to enhance the crystallinity of the film and to increment the proportion of the rutile phase. According to the thermodynamics of the anatase-rutile equilibrium, increasing the temperature tends to favor the rutile growth. This equilibrium is affected by oxygen defects and crystallite size among other factors, changing the transition temperature. Choudhury and Choudhury stated that when the anatase crystallite size is small oxygen defects on grain boundaries are closely packed, interacting with each other and creating a nucleation site for the formation of rutile nuclei [30]. Li et al. found that reducing the anatase particle size (from 23 to 12 nm) lowered the activation energy for phase transition to rutile (from 299 to 180 kJ/mol), thus decreasing the onset transition temperature [31]. Therefore, the crystallization of rutile at relatively low temperature observed in this work can be associated to the small crystallite size of anatase and the presence of oxygen defects.

When a thin Ti interlayer was introduced in the films, the crystallization in rutile was enhanced at both temperatures. This fact suggests that the crystalline structure of the TiO₂ film is also influenced by the Ti microstructure. Analyzing the position of the Ti atoms in the Ti hcp lattice and in the rutile lattice, it can be noticed that the array of Ti atoms in the plane (110) of the rutile is very similar to that of Ti atoms in the (101) and (100) planes of Ti. In the case of the Ti (002) plane, the Ti atom arrangement does not match with the position of the Ti in the rutile lattice. As shown in Figs. 2, 7 and 9, the presence of Ti (002) is noticeable only for Ti films of 315 and 525 nm and the height of these peaks is always significantly lower than that of Ti (100). According to the Ti reference pattern Ti (100) should be less intense than Ti (002) peaks. These results indicate that the Ti films are textured. Knorr et al. noticed a texture development in (101) planes for Ti interlayers with thickness lower than

100 nm deposited at 300 °C and 400 °C by sputtering [32], while Krishna et al. reported that Ti interlayers grown by sputtering at 300 °C with thickness up to 440 nm were textured in (100) planes [22]. In both cases the presence of Ti (002) became more prominent when the thickness was increased. The texture observed in [22,32] was attributed to the contamination of Ti by oxygen during the deposition process. Although Ti (002) plane is the most closely packed, i.e. it has the minimum surface energy, the impurities present in the thin films could alter the surface energy stabilizing other main planes and texturing the film. Taking into account the results reported in the literature and those presented in Fig. 11, it might be inferred that the preferential exposure of Ti (101) and (100) planes on the surface turn rutile the main crystalline phase in the TiO₂ film. Even though the accuracy of the stress analysis could depend on the assumptions made (elastically isotropic lattice and rotational symmetry), within the uncertainties of the method the presence of residual stresses does not seem to be the cause of the Ti lattice expansion. Thus, the increase in the lattice parameters would also be induced by oxygen contamination. The oxygen content in the films could come from oxygen contamination of the Ti cathode or from oxidation of the Ti film surface. Vaquila et al. reported that the oxidation of titanium surface occurs even under high vacuum conditions (~10⁻⁵ Pa) [33] due to the high affinity of titanium to oxygen and the high solid solubility of oxygen in titanium [34]. Wiedermann et al. showed that the oxygen incorporation in the Ti lattice led to a cell expansion proportional to the oxygen content with a relative variation in the parameter *c* higher than in *a*, inducing a distortion of the crystalline lattice of titanium [35]. Results presented in Section 3.2 showed that the Ti cell expansion was more significant when the Ti layer was thinner. This suggests that the oxygen content is relatively higher for the thinnest Ti film. For longer deposition time, the availability of residual oxygen in the chamber decreases, resulting in a lower oxygen concentration. Then, thicker Ti interlayers present a reduction in the lattice distortion. The fact that the thinnest Ti interlayer enhanced the amount of rutile in the TiO₂ film can be associated to the texture and the higher distortion of the Ti lattice. Similar behavior was reported for TiO₂ films deposited by magnetron sputtering on stainless steel substrates with Ti interlayers of different thickness [22]. Authors of ref. [22] related the higher crystallization of rutile phase for the thinnest interlayer with the presence of a higher concentration of oxygen in the Ti layer, incorporated from oxygen residues in the sputter chamber.

5. Conclusions

TiO₂ coatings were prepared by CAD on biased austenitic stainless steel substrates with Ti interlayers of different thickness. It was observed that the introduction of the Ti layer increased the rutile/anatase proportion either at 300 or 400 °C, turning rutile into the main phase in the TiO₂ film. The maximum amount of rutile for each temperature was attained for the thinnest Ti interlayer (55 nm), being larger for 400 °C. The degree of crystallization in the TiO₂ films decreased as the Ti layer thickness increased.

The enhancement in the rutile production by including the Ti interlayer can be attributed to the similarity in the Ti atom positions between the Ti (101) and (100) and the rutile (110) surfaces. Furthermore, oxygen contamination in the titanium, likely greater for thinner layers, seems to induce the inhibition of the Ti (002) surface and the cell expansion –considering that the assumptions of the model employed for stress analysis are fulfilled–, thus promoting the crystallization of TiO₂ especially in the rutile phase.

Acknowledgements

This work was supported by grants of University of Buenos Aires (PID 20020150100103BA) and CONICET (PIP 11220120100468CO).

References

- [1] U. Diebold, The surface science of titanium dioxide, *Surf. Sci. Rep.* 48 (2003) 53–229.
- [2] L. Sirghi, Y. Hatanaka, Hydrophilicity of amorphous TiO₂ ultra-thin films, *Surf. Sci.* 530 (2003) 323–327.
- [3] M.F. Hossain, S. Biswas, T. Takahashi, Y. Kubota, A. Fujishima, Influence of direct current power on the photocatalytic activity of facing target sputtered TiO₂ thin films, *Thin Solid Films* 517 (2008) 1091–1095.
- [4] N. Huang, Y. Chen, J. Luo, J. Yi, R. Lu, J. Xiao, Z. Xue, X. Liu, In vitro investigation of blood compatibility of Ti with oxide layer of rutile structure, *J. Biomater. Appl.* 8 (1994) 404–412.
- [5] N. Huang, P. Yang, Y.X. Leng, J.Y. Chen, H. Sun, J. Wang, G.J. Wang, P.D. Ding, T.F. Xi, Y. Leng, Hemocompatibility of titanium oxide films, *Biomaterials* 24 (2003) 2177–2187.
- [6] C. Larsson, P. Thomsen, J. Lausmaa, M. Rodahl, B. Kasemo, L. Ericson, Bone response to surface modified titanium implants: studies on electropolished implants with different oxide thicknesses and morphology, *Biomaterials* 15 (1994) 1062–1074.
- [7] G. Vallés, P. González-Melendi, J.L. González-Carrasco, L. Saldaña, E. Sánchez-Sabaté, L. Munuera, N. Vilaboa, Differential inflammatory macrophage response to rutile and titanium particles, *Biomaterials* 27 (2006) 5199–5211.
- [8] S. Forberg, Containers for spent nuclear fuel on the corrosion resistance of rutile, *Adv. Ceram.* 20 (1986) 321–327.
- [9] A. Kleiman, A. Márquez, M.L. Vera, J.M. Meichtry, M.I. Litter, Photocatalytic activity of TiO₂ thin films deposited by cathodic arc, *Appl. Catal. B* 101 (2011) 676–681.
- [10] R.L. Boxman, D.M. Sanders, P.J. Martin (Eds.), *Handbook of Vacuum Arc Science and Technology, Fundamentals and Applications*, Noyes Publ, Park Ridge, New Jersey, 1995.
- [11] Y.X. Leng, J.Y. Chen, H. Sun, P. Yang, G.J. Wan, J. Wang, N. Huang, Properties of titanium oxide synthesized by pulsed metal vacuum arc deposition, *Surf. Coat. Technol.* 176 (2004) 141–147.
- [12] P.J. Martin, A. Bendavid, T.J. Kinder, L. Wielunski, The deposition of TiN thin films by nitrogen ion assisted deposition of Ti from a filtered cathodic arc source, *Surf. Coat. Technol.* 86–87 (1996) 271–278.
- [13] A. Kleiman, A. Márquez, H. Kelly, Ion emission in a dc titanium cathodic arc operated with oxygen, *Phys. Scr. T.* 131 (2008), 014005. (4 pp).
- [14] P. Löbl, M. Huppertz, D. Mergel, Nucleation and growth in TiO₂ films prepared by sputtering and evaporation, *Thin Solid Films* 251 (1994) 72–79.
- [15] H. Takikawa, T. Matsui, T. Sakakibara, A. Bendavid, P.J. Martin, Properties of titanium oxide film prepared by reactive cathodic vacuum arc deposition, *Thin Solid Films* 348 (1999) 145–151.
- [16] A. Kleiman, A. Márquez, D.G. Lamas, Anatase TiO₂ films obtained by cathodic arc deposition, *Surf. Coat. Technol.* 201 (2007) 6358–6362.
- [17] A. Bendavid, P.J. Martin, Å. Jamtning, H. Takikawa, Structural and optical properties of titanium oxide thin films deposited by filtered arc deposition, *Thin Solid Films* 355–356 (1999) 6–11.
- [18] F. Zhang, X. Wang, C. Li, H. Wang, L. Chen, X. Liu, Rutile-type titanium oxide films synthesized by filtered arc deposition, *Surf. Coat. Technol.* 110 (1998) 136–139.
- [19] S. Sönmezoglu, G. Çankaya, N. Serin, Phase transformation of nanostructured titanium dioxide thin films grown by sol-gel method, *Appl. Phys. A Mater. Sci. Process.* 107 (2012) 233–241.
- [20] C. Giolli, et al., Characterization of TiO₂ coatings prepared by a modified electric arc-physical vapour deposition system, *Surf. Coat. Technol.* 202 (2007) 13–22.
- [21] L.M. Franco, M.A. Fazio, E. Halac, D. Vega, E. Heredia, A. Kleiman, A. Márquez, Phase transformation of TiO₂ thin films in function bias voltage, *Proc. Mater. Sci.* 8 (2015) 39–45.
- [22] D.S.R. Krishna, Y. Sun, Z. Chen, Magnetron sputtered TiO₂ films on a stainless steel substrate: selective rutile phase formation and its tribological and anti-corrosion performance, *Thin Solid Films* 511 (2011) 4860–4864.
- [23] A. Márquez, G. Blanco, M.E. Fernandez de Rapp, D.G. Lamas, R. Tarulla, Properties of cupric oxide coatings prepared by cathodic arc deposition, *Surf. Coat. Technol.* 187 (2004) 154–160.
- [24] U. Welzel, J. Ligot, P. Lamparter, A.C. Vermuelen, E.J. Mittemeijer, Stress analysis of polycrystalline thin films and surface regions by X-ray diffraction, *J. Appl. Crystallogr.* 38 (2005) 1–29.
- [25] R.C. Chang, F.Y. Chen, C.T. Chuang, Y.C. Tung, Residual stresses of sputtering titanium thin films at various substrate temperatures, *J. Nanosci. Nanotechnol.* 10 (2010) 4562–4567.
- [26] MatWeb, LLC, Matweb - Material Property Data, <http://www.matweb.com> 2017.
- [27] D.A.H. Hanaor, C.C. Sorrell, Review of the anatase to rutile phase transformation, *J. Mater. Sci.* 46 (2011) 855–874.
- [28] G.-R. Gu, Y.-A. Li, Y.-C. Tao, Z. He, J.-J. Li, H. Yin, W.-Q. Li, Y.-N. Zhao, Investigation on the structure of TiO₂ films sputtered on alloy substrates, *Vacuum* 71 (2003) 487–490.
- [29] S.P.S. Porto, P.A. Fleury, T.C. Damen, Raman spectra of TiO₂, MgF₂, ZnF₂, FeF₂, and MnF₂, *Phys. Rev.* 154 (1967) 522–526.
- [30] B. Choudhury, A. Choudhury, Local structure modification and phase transformation of TiO₂ nanoparticles initiated by oxygen defects, grain size, and annealing temperature, *Int. Nano Lett.* 3 (2013) 55.
- [31] W. Li, C. Ni, H. Lin, C.P. Huang, S. Ismat Shah, Size dependence of thermal stability of TiO₂ nanoparticles, *J. Appl. Phys.* 96 (2004) 6663–6668.
- [32] D.B. Knorr, S.M. Merchant, M.A. Biberger, Development of texture in interconnect thin film stacks, *J. Vac. Sci. Technol. B* 16 (1998) 2734–2744.
- [33] I. Vaquila, L.I. Vergara, M.C.G. Passeggi Jr., R.A. Vidal, J. Ferrón, Chemical reactions at surfaces: titanium oxidation, *Surf. Coat. Technol.* 122 (1999) 67–71.
- [34] G. Lütjering, J.C. Williams, *Titanium*, Springer-Verlag, Berlin, 2003.
- [35] K.E. Wiedemann, R.N. Shenoy, J. Unnam, Microhardness and lattice parameter calibrations of the oxygen solid solutions of unalloyed α-titanium and Ti-6Al-2Sn-4Zr-2Mo, *Metall. Trans. A.* 18A (1987) 1503–1510.